PAPER

Effect of Au/HfS₃ interfacial interactions on properties of HfS₃-based devices†

Archit Dhingra, [iD] *[a] Alexey Lipatov, [iD] [bc] Michael J. Loes,[b] Jehad Abourahma,[b] Maren Pink,[d] Alexander Sinitskii [iD] [b] and Peter A. Dowben [iD] [a]

X-ray photoemission spectroscopy (XPS) has been used to examine the interaction between Au and HfS₃ at the Au/HfS₃ interface. XPS measurements reveal dissociative chemisorption of O_2, leading to the formation of an oxide of Hf at the surface of HfS₃. This surface hafnium oxide, along with the weakly chemisorbed molecular species, such as O_2 and H_2O, are likely responsible for the observed p-type characteristics of HfS₃ reported elsewhere. HfS₃ devices exhibit n-type behaviour if measured in vacuum but turn p-type in air. Au thickness-dependent XPS measurements provide clear evidence of band bending as the S 2p and Hf 4f core-level peak binding energies for Au/HfS₃ are found to be shifted to higher binding energies. This band bending implies formation of a Schottky-barrier at the Au/HfS₃ interface, which explains the low measured charge carrier mobilities of HfS₃-based devices. The transistor measurements presented herein also indicate the existence of a Schottky barrier, consistent with the XPS core-level binding energy shifts, and show that the bulk of HfS₃ is n-type.

Introduction

HfS₃ belongs to the family of transition metal trichalcogenides (TMTs) of the form MX₃ (where M = Ti, Zr, Hf, Ta, etc.; and X = S, Se, Te),[1–6] which are two-dimensional (2D) van der Waals materials having quasi-one-dimensional (quasi-1D) chains. Their peculiar quasi-1D chains make them attractive candidates for a myriad of nanodevice applications,[7–14] as they are free from undesirable edge disorders that have afflicted other 2D materials like graphene,[15,16] its derivatives,[17] and transition metal dichalcogenides.[18–23]

What makes HfS₃ stand out among its titanium and zirconium counterparts is the high Z of hafnium, which would result in appreciable intrinsic spin–orbit coupling (SOC) in HfS₃. The enhanced intrinsic SOC in HfS₃ may be exploited for potential spintronics applications.[24] Besides, HfS₃ also has the potential for optoelectronic applications in the ultraviolet-visible range.[14,25] However, as is the case with most 2D materials, the interactions at the metal–TMT interface need to be thoroughly investigated before TMT-based devices can be successfully fabricated; and in

the case of the TMT semiconductors, band alignments can be quite complex.[26] This is because contact related problems are among the fundamental challenges that limit the reliable determination of key performance indicators of 2D devices,[27,28] like the charge carrier mobility. For example, the formation of a Schottky barrier[29] at the interface between Au and In₄Se₃,[30] which is another TMT, has resulted in low carrier mobilities. In other words, establishing the exact nature of electrical contacts at the metal(Au)–TMT(HfS₃) interface is crucial.

It cannot be assumed that the different TMTs behave in a similar fashion as there is a recent experimental demonstration that the mobility of ZrS₃ is orders of magnitude smaller than TiS₃.[31] In the case of TiS₃, Au forms largely an Ohmic contact,[31] while for ZrS₃, Au forms a non-Ohmic contact.[32] This is a little unexpected since both TiS₃ and ZrS₃ are n-type semiconductors[33,34] and gold has a large work function.[35–37] Moreover, further evidence is needed to ascertain the true semiconducting character of HfS₃, since Xiong *et al.*[25] claim that HfS₃ is a p-type semiconductor while Flores *et al.*[38] showed that it is an n-type semiconducting material.

In this work, we have used Au thickness-dependent X-ray photoemission spectroscopy (XPS) to probe the interaction at the Au/HfS₃ interface to determine whether the Au contacts are Ohmic. We have also performed electrical transport measurements on HfS₃ transistors to elucidate its semiconducting behaviour.

Experimental details

The HfS₃ crystals were synthesized through a reaction between metallic hafnium and sulfur vapor in vacuum-sealed quartz ampules at 600 °C, as has been described previously.[39] After two

[a] *Department of Physics and Astronomy, Theodore Jorgensen Hall, University of Nebraska-Lincoln, 855 N 16th Street, Lincoln, Nebraska 68588-0299, USA. E-mail: archit.dhingra@huskers.unl.edu*

[b] *Department of Chemistry, Hamilton Hall, University of Nebraska-Lincoln, 639 North 12th Street, Lincoln, NE 68588-0304, USA*

[c] *Department of Chemistry, Biology & Health Sciences and Karen M. Swindler Department of Chemical and Biological Engineering, South Dakota School of Mines and Technology, 501 E. Saint Joseph St., Rapid City, SD 57701, USA*

[d] *Department of Chemistry, Indiana University, 800 E. Kirkwood Ave., Bloomington, IN 47405-7102, USA*

† Electronic supplementary information (ESI) available. See DOI: https://doi.org/10.1039/d2cp01254e

weeks of annealing at 600 °C, numerous 1–2 mm long HfS_3 crystals were formed. The powder X-ray diffraction (XRD) pattern of HfS_3 was recorded using a PANalytical Empyrean X-ray diffractometer with a 1.4 kW copper K_α source (λ = 1.54187 Å). The powder diffraction patterns were collected from 5° to 150° 2θ using a step size of 0.02° 2θ. HfS_3 is generally isostructural with TiS_3 and ZrS_3,[40,41] and belongs to the $P2_1/m$ space group with the unit cell parameters a = 5.123(2) Å, b = 3.624(1) Å, c = 8.991(1) Å, and the cant angle β = 97.69(2)°, as derived from the powder XRD pattern of HfS_3 shown in Fig. 1. The obtained XRD pattern corresponds to that of pure monoclinic HfS_3, and is consistent with the literature.[25,42]

The XPS measurements were used to characterize the HfS_3 crystal surfaces and interfaces with Au. All the XPS measurements were carried out using an aluminum SPECS X-ray anode (with E(Al Kα) = 1486.6 eV) and a hemispherical electron analyzer (PHI Model: 10-360) in an ultra-high vacuum chamber with a base pressure better than 2×10^{-10} Torr, as mentioned elsewhere.[30] A tungsten wire basket was used to thermally evaporate Au adlayers onto the HfS_3 crystals and a thickness monitor was used to determine their thicknesses, as is described in previous work.[30]

The HfS_3 field-effect transistor (FET) was fabricated using a heavily p-doped Si as the substrate, with a 300 nm thick SiO_2 layer, as the substrate dielectric, and 45 nm thick and 1.5 μm wide pure Au as the source and drain electrodes. The atomic force microscopy (AFM) image of the HfS_3 FET was obtained using a Bruker Dimension Icon atomic force microscope.

The HfS_3-based device was prepared by the standard electron beam lithography using a Zeiss Supra 40 field-emission scanning electron microscope and a Raith pattern generator. The evaporation of Au electrodes was performed using an AJA electron beam evaporation system at the base pressure of $\sim8 \times 10^{-9}$ Torr. For *in vacuo* measurements, the transport data for the HfS_3 FET was measured in a Lake Shore TTPX cryogenic probe station at a base pressure of about 2×10^{-6} Torr; the device was kept in vacuum for several days before the measurements to minimize the effect of surface adsorbates, such as water and oxygen molecules, on the electronic char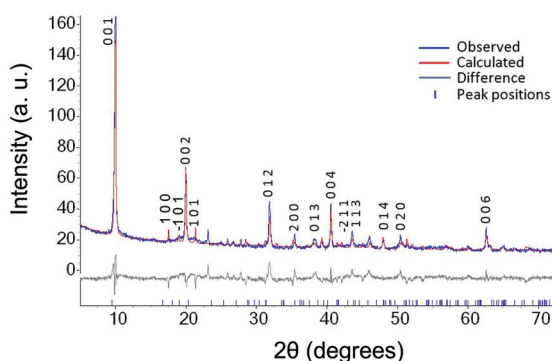acteristics.[43] All the electrical transport measurements for the HfS_3 transistor were carried out under illumination by a halogen lamp to maximize conductance, as indicated by prior work.[25]

Results and discussion

The survey XPS spectrum of bare HfS_3 single crystals showing all the major peaks is presented in Fig. 2(a). The S 2p and Hf 4f core-level peaks belong to the HfS_3 crystals, whereas the Mo 3d and Cu LMM (Auger electron transition) peaks are attributed to the sample holder. The C 1s peak is characteristic of the conductive carbon tape on which the HfS_3 crystals were mounted and the O 1s peak has to do with the surface oxidation of these crystals (this is discussed in more detail below). Further analysis of the raw S 2p core-level XPS spectrum (Fig. 2(b)) indicates that it includes four S 2p components: S^{2-} $2p_{3/2}$ (161 ± 0.1 eV), S^{2-} $2p_{1/2}$ (162.2 ± 0.1 eV), S_2^{2-} $2p_{3/2}$ (162.2 ± 0.1 eV) and S_2^{2-} $2p_{1/2}$ (163.4 ± 0.1 eV). The binding energy values of these four S 2p core-level components are in agreement with the binding energies of the four S 2p core-level components of TiS_3 and ZrS_3, which is to be expected since HfS_3 is isostructural with TiS_3 and ZrS_3.[41] Fig. 2(c) shows the raw (red triangles) and fitted (solid black) XPS spectrum of the Hf 4f core-level. The fit results disclose that the Hf 4f core-level XPS spectrum contains two Hf $4f_{7/2}$ peaks and two Hf $4f_{5/2}$ peaks, with the spin–orbit splitting between each doublet being ~1.7 eV. The Hf $4f_{7/2}$ core-level peak observed at 16.0 ± 0.1 eV and the Hf $4f_{5/2}$ core-level peak observed at 17.7 ± 0.1 eV are attributed to the Hf–S bonding environment, whereas the Hf $4f_{7/2}$ core-level peak observed at 16.7 ± 0.1 eV and the Hf $4f_{5/2}$ core-level peak observed at 18.4 ± 0.1 eV are attributed to the Hf–O bonding environment. The Hf $4f_{7/2}$ peak observed at 16.7 ± 0.1 eV is consistent with the binding energy of Hf $4f_{7/2}$ core-level of HfO_2,[44–48] implying chemisorption of O_2 at the HfS_3 surface. This result is noteworthy in that even though the dissociative adsorption of O_2 on HfS_3 was already implied by Xiong *et al.*,[25] its precise nature was not clarified.

Fig. 3(a) shows the XPS survey scan of HfS_3 with 18 Å of Au at its surface. On comparing this survey XPS with the survey XPS of bare HfS_3 (shown in Fig. 2(a)), it can be inferred that the XPS signal intensity for Au(18 Å)/HfS_3 is dominated by Au. This, however, is not surprising as XPS is a surface sensitive technique with sampling depths of only a few nanometres.[49,50] Fig. 3(b) and (c) show the Au thickness-dependent representative photoemission spectra of the S 2p and Hf 4f core-levels, respectively. In these figures, a clear shift of ~0.8 eV to higher binding energies for both the core-levels is observed upon interfacing HfS_3 with 6 Å of Au (blue). No further shift in the binding energies of the XPS core levels of HfS_3 is observed upon increasing the Au adlayer thickness. That is to say, the XPS peaks of the S 2p and Hf 4f core levels of Au/HfS_3 are shifted by ~0.8 eV towards higher binding energies for all coverages of Au [*i.e.*, 6 Å (blue), 12 Å (green), and 18 Å (purple)] in comparison with their peaks for the bare HfS_3. Therefore, this shift to the higher binding energies for both the core levels is independent
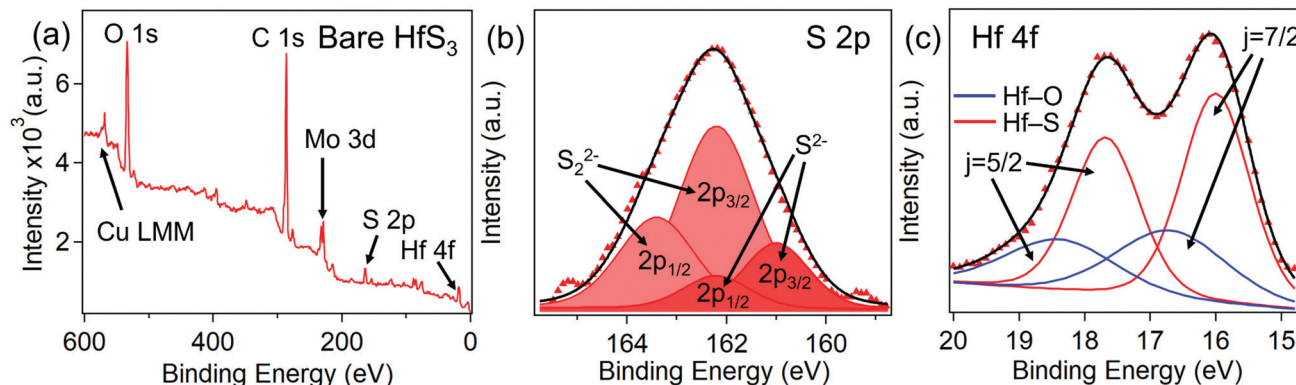

Fig. 1 The powder XRD pattern of HfS_3 accompanied by the Rietveld analysis. Here, peak positions are matched with the prior XRD (ICSD-42074).[1]

Fig. 2 XPS of bare HfS_3. (a) Survey XPS of bare HfS_3 with S 2p and Hf 4f core-level peaks of HfS_3. The Mo 3d core-level peak and Cu LMM (Auger electron transition) peak are due to the sample holder, while the C 1s and O 1s core-level peaks are attributed to adventitious contamination. (b) The raw XPS spectrum of the S 2p core-level (red triangles) along with the fits (shaded in red) showing the S^{2-} $2p_{3/2}$ (161 eV), S^{2-} $2p_{1/2}$ (162.2 eV), S_2^{2-} $2p_{3/2}$ (162.2 eV) and S_2^{2-} $2p_{3/2}$ (163.4 eV) core-level components. The total fit to the raw XPS spectrum of the S 2p core-level is shown in solid black. (c) Raw photoemission spectrum of the Hf 4f core-level (red triangles) along with the total fit to the raw spectrum (solid black). The Hf $4f_{7/2}$ (16.0 eV) and Hf $4f_{5/2}$ (17.7 eV) core-level peaks (in red) are attributed to the Hf–S bonding environment, while the Hf $4f_{7/2}$ (16.7 eV) and Hf $4f_{5/2}$ (18.4 eV) core-level peaks (in blue) are attributed to the Hf–O bonding environment.
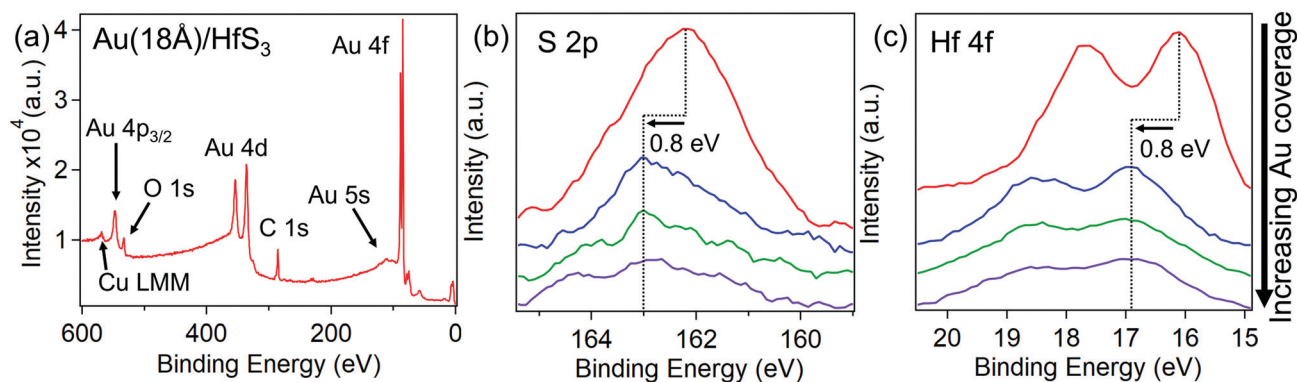

Fig. 3 Au thickness-dependent XPS of HfS_3. (a) Survey XPS of HfS_3 with 18 Å of Au adlayer thickness. (b) The S 2p and (c) Hf 4f core-level photoemission spectra as a function of Au adlayer thickness. Here, the spectra shown in red, blue, green, and purple were collected for 0 Å of Au coverage (i.e., bare HfS_3), 6 Å of Au coverage, 12 Å of Au coverage and 18 Å of Au coverage, respectively. The vertical dashed lines denote the peak XPS binding energies of the S 2p and Hf 4f core-levels, and the horizontal dashed line denotes the shift (of ~0.8 eV) in their respective binding energies.

of the Au adlayer thickness (unlike what was recently observed when different thicknesses of Au adlayers were deposited on ZrS_3[32]). In the absence of surface charging, such a shift towards higher binding energies implies this is an interface effect associated with some band bending.

Such a shift, towards higher binding energies (or lower electron energies), implies downward bending of the conduction and valence bands of HfS_3 at the surface. And it is well-known that downward band bending is indicative of a Schottky-barrier formation at the metal/p-type semiconductor interface.[29,51–53] Therefore, our Au thickness-dependent XPS measurements confirm the existence of a potential (Schottky) barrier at the Au/HfS_3 interface.[25] Existence of a Schottky barrier at the Au/HfS_3 interface, as opposed to its absence at the Au/ZrS_3[32] and Au/TiS_3[31] interfaces, can be explained in terms of varying metal–sulphur interactions among the family of TMTs. In other words, the stronger the TMT metal–sulfur interaction, the weaker the Au–S interaction. Since the

electronegativity of Hf is lower than that of both Zr and Ti, the Au–S interaction at the Au/HfS_3 interface is weaker than it is at either the Au/ZrS_3 or Au/TiS_3 interface. Thus, the absence of a strong Au–S interfacial interaction (presence of which suppresses Schottky-barrier formation at the Au/ZrS_3 and Au/TiS_3 interfaces) results in the formation of a Schottky barrier at the Au/HfS_3 interface. Additionally, these measurements suggest that the work function of the HfS_3 surface with chemisorbed oxygen (see Fig. S1, ESI†) may be higher than that of Au; otherwise, formation of a p-type Schottky barrier at the Au/HfS_3 interface would not be possible.[54–56] This is consistent with theory,[26] which indicates that the work function of HfS_3 (~5.5 eV) is actually higher than that of Au (~5.1 eV).[37]

The HfS_3 FET is schematically shown in Fig. 4(a), which shows a relatively thin p-type surface of HfS_3 that forms due to dissociative chemisorption of oxygen species on n-type HfS_3. The AFM image of the HfS_3 FET with pure Au electrodes that
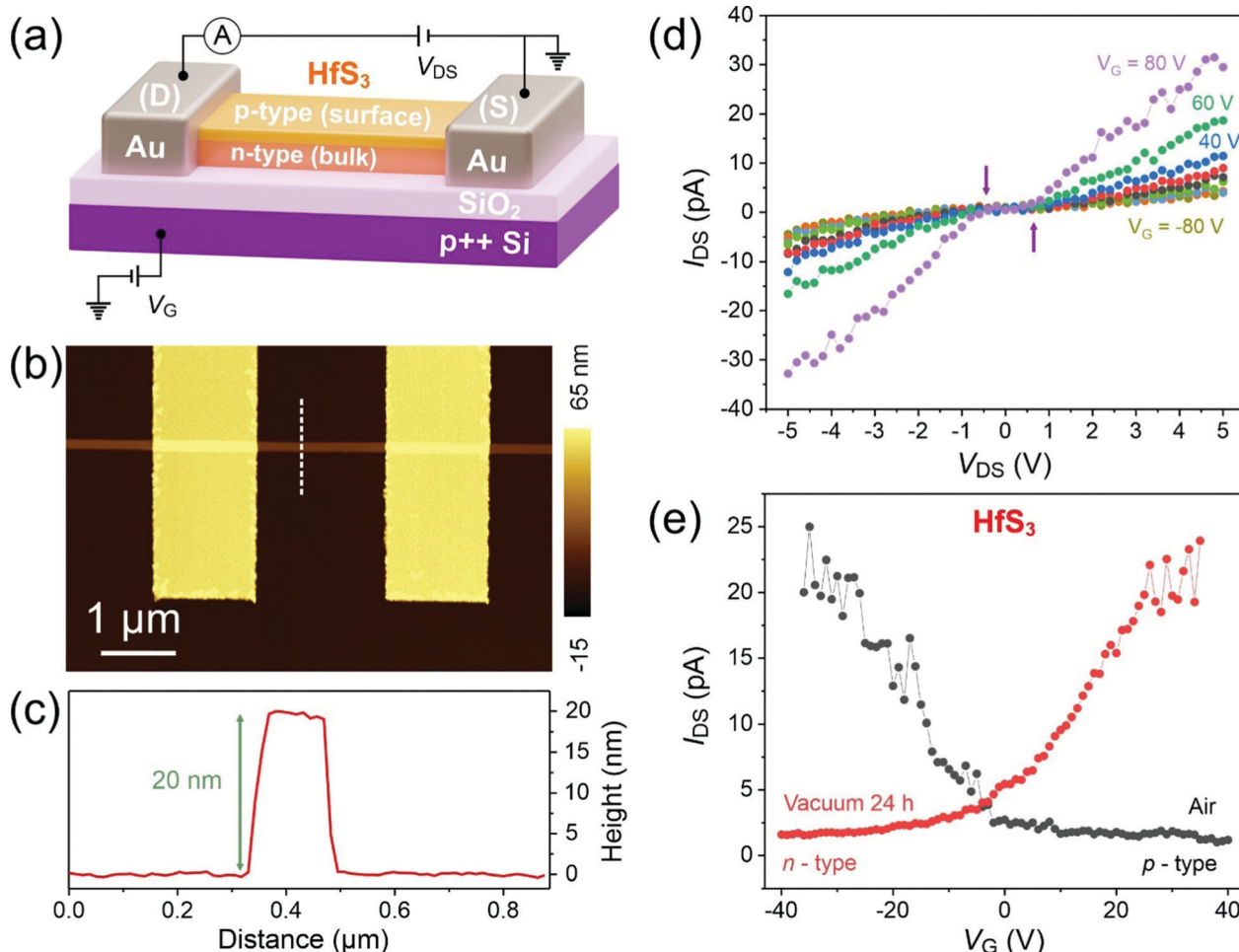
Fig. 4 Electrical transport measurements of the HfS$_3$ FET. (a) Schematic of the HfS$_3$ FET. In addition to the geometry of the electrodes and the device channel, it also (rather exaggeratively) shows a relatively thin p-type surface of a material whose bulk is n-type. The p-type surface is formed because of chemisorption of oxygen on the n-type HfS$_3$, as is evident from Fig. 2(c). (b) AFM image of the HfS$_3$ FET and (c) its corresponding height profile. (d) The I_{DS}–V_{DS} curves of the HfS$_3$ FET measured in vacuum at the gate voltages (V_G) varied from −80 V to +80 V. (e) Transfer characteristics of the same device measured in air (black) and in vacuum (red). V_{DS} = 5 V.

are 45 nm thick is shown in Fig. 4(b). Its height profile (Fig. 4(c)) shows that the HfS$_3$ semiconductor channel is about 20 nm high and 0.2 μm wide. Fig. 4(d) shows the dependence of the drain–source current (I_{DS}) on the drain–source bias (V_{DS}) for gate voltage (V_G) ranging from −80 V to +80 V. The negligible drain–source current, at all the gate voltages, for drain–source voltages between (approximately) −0.3 V to +0.3 V is consistent with the Schottky-barrier formation, as unveiled by our XPS measurements; changes in the slopes of the I_{DS}–V_{DS} plots are indicated by the vertical arrows. The electronic properties of a HfS$_3$ device depend on the background ambience. In vacuum, from the direct relationship between I_{DS} and V_G, which is evident from the increasing I_{DS} with increasing V_G at a given V_{DS} (see the red curve in Fig. 4(e)), that in spite of a p-type surface layer HfS$_3$ is an n-type semiconducting material similar to TiS$_3$.[57,58] When the same device is measured in air, HfS$_3$ exhibits p-type behaviour, as shown by the black curve in Fig. 4(e). As placing the HfS$_3$ FET device *in vacuo*, at about 2×10^{-6} Torr, for 24 h results in the restoration the n-type

electronic behavior (again, see the red curve in Fig. 4(e)), much of the p-type doping has to be the result of weakly bound adsorbate species, such as H$_2$O and O$_2$, on the surface of HfS$_3$. This is not surprising since adsorbates like H$_2$O and O$_2$ are known for their p-doping effect on other 2D materials, such as graphene oxide.[43] The Schottky-barrier formation seen in XPS (Fig. 3(c)), in combination with the p–n junction formed between the p-type surface and the n-type bulk, and the overall transport characteristics at large source drain voltages (Fig. 4(d)) are also consistent with the very low currents ($\sim 10^{-11}$ A) measured here. Even though the I–V characteristics for the HfS$_3$ FET were measured in the presence of illumination, the observed currents are still far less than what is seen for similar ZrS$_3$ ($\sim 10^{-7}$ A) and TiS$_3$ ($\sim 10^{-6}$ A) FET devices in the absence of illumination.[40] A comparison of the conductivity for the HfS$_3$ devices, in absence of irradiation, would be even more invidious.

Although, to date, HfS$_3$ is the first TMT whose surface semiconducting character is shown to be different from its

bulk semiconducting behaviour, there have been precedents of other semiconductors where surfaces were found to differ from their bulk.[59–63] The above discussions are summarized in Fig. 4(a). Again, we note that the p-type behaviour at surface of HfS$_3$ can become more significant because of the further weak chemisorption due to the ambient air.

Conclusions

In conclusion, facile chemisorption of oxygen is manifested in our XPS measurements on bare HfS$_3$, which renders its surface p-type. Our XPS data also confirms the formation of a Schottky barrier at the Au/HfS$_3$ interface, which is independent of the Au adlayer thickness. This barrier, in combination with the p–n junction formed between the p-type surface and the n-type bulk, is responsible for the poor $I–V$ characteristics of a HfS$_3$-based device fabricated with Au contacts. This is, indeed, in agreement with the observed low source–drain current reported herein (and elsewhere[25]). Our *in vacuo* electrical transport measurements demonstrate n-type semiconducting behaviour for the as-synthesized HfS$_3$, indicative of sulphur vacancies.[3,4] Therefore, our study shows clear evidence for the existence of a Schottky barrier at the Au/HfS$_3$ interface, in addition to conveying that the surface of HfS$_3$ is p-type while its bulk is n-type. The intriguing presence of a p-type surface and an n-type bulk reconciles a prior experimental study reporting the p-type characteristics of HfS$_3$[25] with another experimental report on the intrinsic n-type semiconducting nature of this material.[38]

Data availability

The data that support the findings of this study are available from the corresponding author upon reasonable request.

Author contributions

A. D. and P. A. D. conceived the idea and coordinated this work. A. S. supervised the sample preparation and structural characterization. A. L. and J. A. prepared the HfS$_3$ crystals. A. L. fabricated the HfS$_3$ devices, wrote a software code and performed electrical measurements on the devices, and analyzed the results. M. J. L. performed AFM characterization and analysis. M.P. performed XRD measurements and analysis. A. D. performed XPS measurements and analysis. A. D., A. S. and P. A. D. co-wrote the manuscript. A. D. and A. L. prepared the figures. All authors have given approval to the final version of the manuscript.

Conflicts of interest

There are no conflicts to declare.

Acknowledgements

Notes and references

1 S. Furuseth, L. Brattas and A. Kjekshus, *Acta Chem. Scand.*, 1975, **29**, 623–631.

2 S. K. Srivastava and B. N. Avasthi, *J. Mater. Sci.*, 1992, **27**, 3693–3705.

3 J. Dai, M. Li and X. C. Zeng, *Wiley Interdiscip. Rev.: Comput. Mol. Sci.*, 2016, **6**, 211–222.

4 J. O. Island, M. Barawi, R. Biele, A. Almazán, J. M. Clamagirand, J. R. Ares, C. Sánchez, H. S.-J. van der Zant, J. V. Álvarez, R. D'Agosta, I. J. Ferrer and A. Castellanos-Gomez, *Adv. Mater.*, 2015, **27**, 2595–2601.

5 A. Lipatov, M. J. Loes, H. Lu, J. Dai, P. Patoka, N. S. Vorobeva, D. S. Muratov, G. Ulrich, B. Kästner, A. Hoehl, G. Ulm, X. C. Zeng, E. Rühl, A. Gruverman, P. A. Dowben and A. Sinitskii, *ACS Nano*, 2018, **12**, 12713–12720.

6 J. Dai and X. C. Zeng, *Angew. Chem., Int. Ed.*, 2015, **54**, 7572–7576.

7 F. Saiz, J. Carrete and R. Rurali, *Nanomaterials*, 2020, **10**, 704.

8 Y. Jin, X. Li and J. Yang, *Phys. Chem. Chem. Phys.*, 2015, **17**, 18665–18669.

9 J. O. Island, A. J. Molina-Mendoza, M. Barawi, R. Biele, E. Flores, J. M. Clamagirand, J. R. Ares, C. Sánchez, H. S.-J. van der Zant, R. D'Agosta, I. J. Ferrer and A. Castellanos-Gomez, *2D Mater.*, 2017, **4**, 022003.

10 A. Patra and C. S. Rout, *RSC Adv.*, 2020, **10**, 36413–36438.

11 X. Yu, X. Wen, W. Zhang, L. Yang, H. Wu, X. Lou, Z. Xie, Y. Liu and H. Chang, *CrystEngComm*, 2019, **21**, 5586–5594.

12 S. Hou, Z. Guo, J. Yang, Y. Liu, W. Shen, C. Hu, S. Liu, H. Gu and Z. Wei, *Small*, 2021, 2100457.

13 A. Dhingra, S. J. Gilbert, J.-S. Chen, P. V. Galiy, T. M. Nenchuk and P. A. Dowben, *MRS Adv.*, 2022, DOI: **10.1557/s43580-022-00259-6**.

14 Y. R. Tao, J. J. Wu and X. C. Wu, *Nanoscale*, 2015, **7**, 14292–14298.

15 E. R. Mucciolo and C. H. Lewenkopf, *J. Phys.: Condens. Matter*, 2010, **22**, 273201.

16 F. Banhart, J. Kotakoski and A. V. Krasheninnikov, *ACS Nano*, 2010, **5**, 26–41.

17 R. Debbarma, N. H.-L. Nguyen and V. Berry, *Appl. Mater. Today*, 2021, **23**, 101072.

18 H.-P. Komsa, J. Kotakoski, S. Kurasch, O. Lehtinen, U. Kaiser and A. V. Krasheninnikov, *Phys. Rev. Lett.*, 2012, **109**, 035503.

19 S.-T. Lo, O. Klochan, C.-H. Liu, W.-H. Wang, A. R. Hamilton and C.-T. Liang, *Nanotechnology*, 2014, **25**, 375201.

20 R. Addou, L. Colombo and R. M. Wallace, *ACS Appl. Mater. Interfaces*, 2015, **7**, 11921–11929.

21 Z. Lin, B. R. Carvalho, E. Kahn, R. Lv, R. Rao, H. Terrones, M. A. Pimenta and M. Terrones, *2D Mater.*, 2016, **3**, 022002.

22 M. R. Rosenberger, H.-J. Chuang, K. M. McCreary, C. H. Li and B. T. Jonker, *ACS Nano*, 2018, **12**, 1793–1800.

23 W. H. Blades, N. J. Frady, P. M. Litwin, S. J. McDonnell and P. Reinke, *J. Phys. Chem. C*, 2020, **124**, 15337–15346.

24 I. Žutić, J. Fabian and S. Das Sarma, *Rev. Mod. Phys.*, 2004, **76**, 323–410.

25 W. W. Xiong, J. Q. Chen, X. C. Wu and J. J. Zhu, *J. Mater. Chem. C*, 2014, **2**, 7392–7395.

26 Q. Zhao, Y. Guo, Y. Zhou, Z. Yao, Z. Ren, J. Bai and X. Xu, *Nanoscale*, 2018, **10**, 3547–3555.

27 D. S. Schulman, A. J. Arnold and S. Das, *Chem. Soc. Rev.*, 2018, **47**, 3037–3058.

28 L.-W. Wong, L. Huang, F. Zheng, Q. H. Thi, J. Zhao, Q. Deng and T. H. Ly, *Nat. Commun.*, 2020, **11**, 1–10.

29 Z. Zhang and J. T. Yates, *Chem. Rev.*, 2012, **112**, 5520–5551.

30 A. Dhingra, P. V. Galiy, L. Wang, N. S. Vorobeva, A. Lipatov, A. Torres, T. M. Nenchuk, S. J. Gilbert, A. Sinitskii, A. J. Yost, W.-N. Mei, K. Fukutani, J.-S. Chen and P. A. Dowben, *Semicond. Sci. Technol.*, 2020, **35**, 065009.

31 S. J. Gilbert, A. Lipatov, A. J. Yost, M. J. Loes, A. Sinitskii and P. A. Dowben, *Appl. Phys. Lett.*, 2019, **114**, 101604.

32 A. Dhingra, A. Lipatov, A. Sinitskii and P. A. Dowben, *J. Phys.: Condens. Matter*, 2021, **33**, 434001.

33 H. Yi, T. Komesu, S. Gilbert, G. Hao, A. J. Yost, A. Lipatov, A. Sinitskii, J. Avila, C. Chen, M. C. Asensio and P. A. Dowben, *Appl. Phys. Lett.*, 2018, **112**, 052102.

34 H. Yi, S. J. Gilbert, A. Lipatov, A. Sinitskii, J. Avila, J. Abourahma, T. Komesu, M. C. Asensio and P. A. Dowben, *J. Phys.: Condens. Matter*, 2020, **32**, 29LT01.

35 D. E. Eastman, *Phys. Rev. B: Condens. Matter Mater. Phys.*, 1970, **2**, 1–2.

36 H. C. Potter and J. M. Blakely, *J. Vac. Sci. Technol.*, 1975, **12**, 635–642.

37 H. Kawano, *Prog. Surf. Sci.*, 2008, **83**, 1–165.

38 E. Flores, J. R. Ares, I. J. Ferrer and C. Sánchez, *Phys. Status Solidi RRL*, 2016, **10**, 802–806.

39 H. Haraldsen, A. Kjekshus, E. Røst, A. Steffensen and J. Munch-Petersen, *Acta Chem. Scand.*, 1963, **17**, 1283–1292.

40 S. J. Gilbert, H. Yi, J.-S. Chen, A. J. Yost, A. Dhingra, J. Abourahma, A. Lipatov, J. Avila, T. Komesu, A. Sinitskii, M. C. Asensio and P. A. Dowben, *ACS Appl. Mater. Interfaces*, 2020, **12**, 40525–40531.

41 A. Dhingra, A. Lipatov, M. J. Loes, A. Sinitskii and P. A. Dowben, *ACS Mater. Lett.*, 2021, **3**, 414–419.

42 Y.-R. Tao, J.-Q. Chen, J.-J. Wu, Y. Wu and X.-C. Wu, *J. Alloys Compd.*, 2016, **658**, 6–11.

43 A. Sinitskii, A. Dimiev, D. V. Kosynkin and J. M. Tour, *ACS Nano*, 2010, **4**, 5405–5413.

44 D. D. Sarma and C. N.-R. Rao, *J. Electron Spectrosc. Relat. Phenom.*, 1980, **20**, 25–45.

45 G. D. Wilk, R. M. Wallace and J. M. Anthony, *J. Appl. Phys.*, 1999, **87**, 484.

46 H. Y. Yu, M. F. Li, B. J. Cho, C. C. Yeo, M. S. Joo, D.-L. Kwong, J. S. Pan, C. H. Ang, J. Z. Zheng and S. Ramanathan, *Appl. Phys. Lett.*, 2002, **81**, 376.

47 N. Zhan, M. C. Poon, C. W. Kok, K. L. Ng and H. Wong, *J. Electrochem. Soc.*, 2003, **150**, F200.

48 D. Barreca, A. Milanov, R. A. Fischer, A. Devi and E. Tondello, *Surf. Sci. Spectra*, 2007, **14**, 34.

49 S. D. Gardner, C. S.-K. Singamsetty, G. L. Booth, G.-R. He and C. U. Pittman, *Carbon*, 1995, **33**, 587–595.

50 J. B. Gilbert, M. F. Rubner and R. E. Cohen, *Proc. Natl. Acad. Sci. U. S. A.*, 2013, **110**, 6651–6656.

51 T. U. Kampen and W. Mönch, *Surf. Sci.*, 1995, **331–333**, 490–495.

52 G. Song, M. Y. Ali and M. Tao, *IEEE Electron Device Lett.*, 2007, **28**, 71–73.

53 D. A. Svintsov, A. V. Arsenin and D. Y. Fedyanin, *Opt. Express*, 2015, **23**, 19358.

54 R. E. Thomas, *Solar Energy Conversion*, Elsevier, 1979, pp. 805–830.

55 K. C. Kao, *Dielectric Phenomena in Solids*, Elsevier, 2004, pp. 327–380.

56 A. Hussain and A. Rahman, *Mater. Sci. Semicond. Process.*, 2013, **16**, 1918–1924.

57 A. Lipatov, P. M. Wilson, M. Shekhirev, J. D. Teeter, R. Netusil and A. Sinitskii, *Nanoscale*, 2015, **7**, 12291–12296.

58 M. Randle, A. Lipatov, A. Kumar, C.-P. Kwan, J. Nathawat, B. Barut, S. Yin, K. He, N. Arabchigavkani, R. Dixit, T. Komesu, J. Avila, M. C. Asensio, P. A. Dowben, A. Sinitskii, U. Singisetti and J. P. Bird, *ACS Nano*, 2018, **13**, 803–811.

59 R. H. Kingston, *Phys. Rev.*, 1955, **98**, 1766–1775.

60 R. E. Jones, K. M. Yu, S. X. Li, W. Walukiewicz, J. W. Ager, E. E. Haller, H. Lu and W. J. Schaff, *Phys. Rev. Lett.*, 2006, **96**, 125505.

61 J. H. Song, T. Akiyama and A. J. Freeman, *Phys. Rev. Lett.*, 2008, **101**, 186801.

62 C. A. Hurni, S. Choi, O. Bierwagen and J. S. Speck, *Appl. Phys. Lett.*, 2012, **100**, 082106.

63 L. Maserati, I. Moreels, M. Prato, R. Krahne, L. Manna and Y. Zhang, *ACS Appl. Mater. Interfaces*, 2014, **6**, 9517–9523.

This journal is © the Owner Societies 2022

Phys. Chem. Chem. Phys., 2022, **24**, 14016–14021 | **14021**